Atmospheric Pollution Research 13 (2022) 101451

Contents lists available at ScienceDirect

Atmospheric Pollution Research

journal homepage: www.elsevier.com/locate/apr

Defining the upper boundary of the Asian Tropopause Aerosol Layer (ATAL) using the static stability

S.T. Akhil Raj [a,*], M. Venkat Ratnam [a], J.P. Vernier [b,c], A.K. Pandit [b], Frank G. Wienhold [d]

[a] National Atmospheric Research Laboratory, Gadanki, India
[b] National Institute of Aerospace, Hampton, VA, USA
[c] NASA Langley Research Center, USA
[d] Institute of Atmospheric and Climate Science, Universitaetstrasse 16, Zurich, Switzerland

ARTICLE INFO

Keywords:
ATAL
UTLS region
BATAL
Asian summer monsoon anticyclone

ABSTRACT

The Asian Tropopause Aerosol Layer (ATAL) is located in the Upper Troposphere and Lower Stratosphere (UTLS) during the Asian Summer Monsoon. However, what dynamical feature separates the ATAL from the well-known stratospheric 'Junge layer' is not yet clear. In this study, using the in-situ (Radiosonde, Ozonesonde, backscatter sonde and cryogenic frost-point hygrometer) observations from multiple locations in India (Gadanki (13.45° N, 79.18° E), Hyderabad (17.47° N, 78.58° E) and Varanasi (25.27° N, 82.99° E)) and multi-satellite observations ((Cloud-Aerosol Lidar and Infrared Pathfinder Observation, (CALIPSO), Atmospheric Chemistry Experiment (ACE) Fourier Transform Spectrometer (FTS) and Constellation Observation System for Meteorology, Ionosphere and Climate (COSMIC) Global Position System (GPS) Radio Occultation (RO) (COSMIC GPS-RO)) we show that the ATAL can exist up to the layer of maximum stability (LmaxS), located a few kilometers above the tropopause, determined using the square of Brunt Väisäla frequency. These in-situ observations over Indian stations collected during the ISRO-NASA Balloon Measurement Campaigns of the Asian Tropopause Aerosol Layer (BATAL) show that the ATAL top can reach up to ~442 K potential temperature level over the Indian region. The LmaxS delineated from COSMIC GPSRO observations over the Asian Summer Monsoon Anticyclone (ASMA) region indicates that the top of ATAL can reach up to 454 K potential temperature level, which is lower than the earlier Lagrangian transport model predicted 460 K. The temperature inversion at LmaxS acts as a lid and constrains the direct transport of aerosols to higher altitudes.

1. Introduction

The Asian Summer Monsoon Anticyclone (ASMA), a major dynamical system extending from the upper troposphere to the lower stratosphere during the boreal summer is known to contain an enhanced concentration of tropospheric pollutants, either lifted by the associated deep convection over the Indian subcontinent (Hoskins and Rodwell, 1995) or through long-range transport (Brunamonti et al., 2018; Vogel et al., 2019; Basha et al., 2020, 2021). The quasi-persistence of anticyclone in the UTLS region results in the accumulation of tropospheric trace gases (H_2O, CH_4, CO etc.) and a reduction in the stratospheric trace gases (in O_3, HNO_3, HCl, etc.) within the ASMA (Park et al., 2008, 2013; Randel et al., 2010; Garny and Randel, 2016; Basha et al., 2021). However, the existence of the Asian Tropopause Aerosol Layer (ATAL) in the ASMA region was discovered using Cloud-Aerosol Lidar and Infrared Pathfinder Satellite Observations (CALIPSO) mission a few years later (Vernier et al., 2011, 2015). Further, the existence of ATAL from 1999 onwards is observed in the Stratospheric Aerosols and Gas Experiments (SAGE) II measurements (Thomason and Vernier, 2013). However, the spatially resolved Ammonium Nitrate (NH_4NO_3, (AN)) observations with Cryogenic Infrared Spectrometers and Telescopes for the Atmosphere (CRISTA) showed enhanced concentrations of solid AN in the upper troposphere within the ASMA as early as 1997 (Höpfner et al., 2019). The ATAL occur between ~360 K and ~440 K potential temperature (~13–18 km) from the eastern Mediterranean Sea to western China and India with a thickness of 3–4 km around 30–40° N and thinner near the equator (Vernier et al., 2011, 2015, 2018; Hanumanthu et al., 2020; Bian et al., 2020). The UTLS aerosols long-term observations

Peer review under responsibility of Turkish National Committee for Air Pollution Research and Control.
* Corresponding author.
E-mail address: akhil@narl.gov.in (S.T.A. Raj).

https://doi.org/10.1016/j.apr.2022.101451
Received 21 January 2022; Received in revised form 6 May 2022; Accepted 6 May 2022
Available online 12 May 2022
1309-1042/

suggest that the ATAL optical depth has increased 2–3 times since the late 1990 (Vernier et al., 2018). The satellite observations of ATAL were consistent with the early balloon-borne observations made from Lhasa (29.7° N, 91.1° E) in August 1999 (Kim et al., 2003; Hanumanthu et al., 2020). The first offline chemical analysis during the Balloon Measurement Campaigns of the Asian Tropopause Aerosol Layer (BATAL) using ion chromatography (IC) suggests that the nitrate is a more important chemical component of the ATAL than the sulphate aerosols, which were lower than the IC detection limit (Vernier et al., 2018). This observation was consistent with the model results of Gu et al. (2016). These results are further supported by the later observations of AN from CRISTA and ammonia (NH_3) observed using Michelson Interferometer for Passive Atmospheric Sounding (MIPAS) (Höpfner et al., 2019). The advanced balloon-borne observations of aerosol over the Indian region using the Compact Optical Backscatter AerosoL Detector (COBALD), Optical Particle Counter (OPC) and offline chemical analysis (IC) shown that the ATAL is mostly composed of relatively small (radius <0.25 μm) liquid (80%–95%) aerosols with relatively low scattering ratio (SR) at 532 nm which is consistent with the CALIPSO observations (Vernier et al., 2018). Independent observations over the ASMA region with balloon-borne aircraft and satellite platforms indicate that the ATAL extends above the cold point tropopause (Vernier et al., 2018; Brunamonti et al., 2018; Hanumanthu et al., 2020; Höpfner et al., 2019; Mahnke et al., 2021; Yu et al., 2017). A relatively high concentration of aerosol is found near the tropopause and declines in the higher altitudes. Particle concentration for radius (r) > 0.094 dominated in the tropopause altitude, with its concentration comparable to that of the boundary layer concentration (up to about 25 particles per cm^{-3}). Particle concentration for r > 0.15 and r > 0.30 μm is smaller by a factor of 30 and 300, respectively. Brunamonti et al. (2018) referred to this extended layer above the cold point tropopause as 'confined lower stratosphere' (CLS) using the 2-week LAGRANTO backward trajectories and water vapor measurements over Nainital, India (29.35° N, 79.46° E) and Dhulikhel, Nepal (27.62° N, 85.54° E). The top of the confined layer is located around 18.6 km (421.5 K) and 19.5 km (441 K) over Nainital and Dhulikhel, respectively. Ma et al. (2022) also observed a similarly mixed layer around 1–1.5 km above the tropopause over ASMA region from the tracer-tracer relationship of O_3 and H_2O. The concept of the confined layer is consistent with the concept of "upward spiralling range" by Vogel et al. (2019). They found that the slow diabatic uplift within the ASMA can transport the airmass up to 460 K from the top of the convective outflow level (~360 K) within a few months. Later these uplifted air masses are transported to a higher altitude via tropical pipe associated with large-scale Brewer-Dobson circulation. The HALO aircraft in-situ observations over extratropical UTLS (15 - 75° N, 25° W-15° E) and 50 days Lagrangian back trajectory analysis also shows a slow diabatic ascent of air mass within the anticyclone up to potential temperature >400 K and subsequent transport to the extratropical lowermost stratosphere (Müller et al., 2016). The analysis of model simulations also shows eddies detached from the anticyclone contribute to transporting the trace gases and aerosols to the western Pacific and western Africa from the Asian region (Fadnavis et al., 2018). The descending motion in the western part (approximately 70° E) is also found to play an important role in the dissipation of the ATAL, in addition to the large scale ascending circulation inside ASMA and the eddy shedding at the east and western edges of the ASMA (He et al., 2020). Aerosol near the tropopause could impact the Earth's radiative balance and the cirrus cloud properties. Based on CALIOP observations between 1995 and 2013, the summertime aerosol optical depth increase within the ATAL resulted in a -1 Wm^2 radiative forcing at the top of the atmosphere. This correspond to the one-third of the total radiative forcing due to increased CO_2 over the same period (Vernier et al., 2015).

ASMA is not a stable, persistent unimodal circulation, it can be bimodal (Tibetan and Iranian modes) with substantial day-to-day variability (Zhang et al., 2002; Vogel et al., 2015, Hemanth Kumar and Ratnam, 2021). There is also considerable interannual variability in the monsoon circulation, which impacts the trace gases and aerosol concentration in the ASMA (Santee et al., 2017, Hemanth Kumar and Ratnam, 2021; Yuan et al., 2019). Hanumanthu et al. (2020) found substantial day-to-day variability of ATAL in both backscatter signal intensity and altitude range. They have also performed Lagrangian back-trajectory analysis to identify the air mass origin in the model boundary layer and its transport pathways to the ATAL over Nainital in August 2016.

There have been many studies exists on ASMA composition, dynamics and ATAL variability in the recent years (Park et al., 2008, 2013; Pan et al., 2016; Santee et al., 2017; Vernier et al., 2015, 2018; Hemanth Kumar and Ratnam, 2021; Yuan et al., 2019; Basha et al., 2020; Hanumanthu et al., 2020; Zhang et al., 2002; Vogel et al., 2015, 2019; He et al., 2020). With Lagrangian models trajectory simulations, few of these studies have shown a slow ascend of air parcels within the anticyclone and reaches an upper boundary of 400–460 K potential temperature (Müller et al., 2016; Vogel et al., 2019; Brunamonti et al., 2018). However, what dynamical aspect separates the ATAL from the well known Jungi layer is not clear. In the present study, we define the upper boundary of the ATAL based on the atmospheric stability, which is derived from the balloon-borne in situ and spaceborne measurements. The rest of the paper is organized as follows. Section 2 outlines the data sets used for the present study. Section 3 comprises the methodology adopted to identify the ATAL top boundary, followed by the description of the results. Summary and discussion are provided in Section 4, and finally, major conclusions for the present study are drawn in Section 5.

2. Data and methodology

In this paper, we used multiple in-situ observations from the BATAL campaign conducted during 2014–2019 (Vernier et al., 2018) and satellite observations to derive the top of the ATAL from the basic atmospheric parameters. The top of the ATAL is delineated based on the static stability criteria (Sunilkumar et al., 2017; Gettelman and Wang, 2015; Birner et al., 2002) using radiosonde observations over Gadanki (13.45° N, 79.18° E), Hyderabad (17.47° N, 78.58° E) and Varanasi (25.27° N, 82.99° E) along with supporting balloon-borne aerosol backscatter, water vapor and ozone observations. The geographical location of the launching sites is shown in Fig. 1, and the details of the sondes used in

Fig. 1. Map showing the balloon launching locations over India during 2014–2019 BATAL Campaigns.

the present study are provided in Table 1. Tropopause parameters and their detection criteria are discussed in section 2.7.

2.1. Radiosonde and ozonesonde

We used both Meisei (RS-11 G) and iMet radiosonde temperature and pressure data as a function of altitude. These radiosondes measure temperature from −90 °C to 50 °C with a resolution of 0.1 °C and accuracy of 0.5 °C at a time resolution of 1s. iMet employs a piezo-resistor to measure atmospheric pressure with an accuracy of ~1–2 hPa between 2 and 1070 hPa. Since the Meisei Radiosonde does not have a pressure sensor, it derives pressure from the observed temperature and GPS altitude with the hypsometric equation. The ozone profile from the surface to the balloon burst altitude (30–35 km) was obtained by the EN-SCI Electrochemical concentration cell (ECC) ozonesondes (Komhyr et al., 1995). Ambient air is bubbled through a cathode chamber filled with potassium iodide solution by a 12 V pump, and the subsequent reaction generates two electrons per ozone molecule. The current measured using an external circuit board later converts into ozone partial pressure with an accuracy of around 5–10%. More details on radiosonde and ozonesonde are available in Ratnam et al. (2014), and Akhil Raj et al. (2015).

2.2. Cryogenic frostpoint hygrometer (CFH)

The CFH is a compact, microprocessor-controlled instrument that operates based on the chilled mirror principle. It accurately measures the frost-point/dew point temperature from the surface to the 28 km altitude range. The CFH operates by precisely controlling the temperature on a small gold-plated oxygen-free high-density copper mirror to generate a thin layer of dew or frost in thermodynamic equilibrium with the ambient air. The thin layer of condensate is maintained by fast heating and cooling with the help of an electrical heater and a cryogenic liquid (Trifluoromethane). A detailed description of the instrument is presented by Vömel et al. (2007). The observed frost point temperature is used to calculate the water vapor mixing ratio by estimating the water vapor partial pressure following the Goff Gratch equation (Goff and Gratch, 1946). CFH measures water vapor with an accuracy of 4% in the lower tropical troposphere, 9% in the tropopause region and 10% in the lower stratosphere. The relative humidity with respect to ice (RH_{ice}) is calculated from the frost point temperature from CFH, and the ambient air temperature measured using iMet radiosonde. RH_{ice} accuracy is 5–7% in the upper troposphere and better than 10% in the lower stratosphere (Sunilkumar et al., 2016).

2.3. Compact Optical Backscatter AerosoL detector (COBALD)

COBALD is a lightweight balloon-borne backscatter sonde developed by ETH Zurich designed to fly with weather balloons operating at optical wavelengths 455 nm (blue) and 940 nm (infrared). Each of these LEDs has an optical power of around 700 mW. A silicon photodiode phase-sensitive detects the light scattered back from air molecules, aerosols or ice particles with an uncertainty of 5% and precision better than 1% in the UTLS region (Vernier et al., 2015, 2018). In the present study, we used the blue backscatter ratio (BSR_{455}) to discern aerosol (ATAL) and cloud, following Hanumanthu et al. (2020). $BSR_{455} < 1.12$ is considered as aerosol, and larger values are treated as cloud/ice particles. We didn't use COBALD observations after August 15, 2017 and 2019 in the present study to avoid the effects of smoke from the Canadian wildfire and Raikoke eruption, respectively.

Table 1
BATAL data used in the present study with a minimum altitude coverage of 22 km. O_3: Ozonesonde, COBALD: Compact Optical Backscatter AerosoL Detector, CFH: Cryogenic Frost-point Hygrometer.

Year	Location	Payloads
2014	Gadanki (13.45° N, 79.18° E)	O_3 (4), COBALD (2)
2015	Gadanki (13.45° N, 79.18° E)	O_3 (1)
2015	Hyderabad (17.47° N, 78.58° E)	O_3 (5), COBALD (6), CFH (5)
2015	Varanasi (25.27° N, 82.99° E)	O_3 (3), COBALD (3), CFH (1)
2016	Gadanki (13.45° N, 79.18° E)	O_3 (6), COBALD (2)
2016	Varanasi (25.27° N, 82.99° E)	COBALD (3)
2017	Gadanki (13.45° N, 79.18° E)	O_3 (1), COBALD (2), CFH (1)
2017	Hyderabad (17.47° N, 78.58° E)	O_3 (6)
2018	Hyderabad (17.47° N, 78.58° E)	O_3 (8), COBALD (5), CFH (3)
2019	Hyderabad (17.47° N, 78.58° E)	O_3 (9), CFH (7)

2.4. Atmospheric Chemistry Experiment (ACE) Fourier Transform Spectrometer (FTS)

We used monthly mean ACE-FTS observations on-board SCISAT between 2014 and 2018 over the ASMA region (10–40° N, 0–120° E). ACE-FTS measure solar spectra from 2.2 to 13.3 μm wavelength using a Michelson interferometer during solar occultations (Bernath et al., 2005). During each occultation, the vertical sampling of each constituent is made with a vertical resolution of 2–6 km depending upon the occultation angle, and the final product is available at a 1 km vertical resolution (Boone et al., 2005). The satellite provides 30 measurements per day for over 30 chemical species from the 5 km–150 km range. Version 3.6 ozone (O_3), water vapor (H_2O), hydrogen cyanide (HCN) and carbon monoxide (CO) observations are used in the present study. The ACE-FTS provides observations primarily over high latitudes with limited measurements over the tropics. Therefore, we have used June-July-August mean profiles within the ASMA region to study the vertical structure of the trace gases and their variation near the tropopause from 2014 to 2018. Though the ACE-FTS provides temperature measurements, we have used high-resolution temperature observations from Constellation Observation System for Meteorology, Ionosphere and Climate (COSMIC) Global Position System (GPS) Radio Occultation (RO) to derive tropopause parameters.

2.5. GPSRO on-board COSMIC satellite

We used temperature profiles retrieved from COSMIC GPSRO obtained during 2014–2018 to derive tropopause parameters over the ASMA region. The temperature and relative humidity profiles are derived from the refractivity profile obtained from the RO method. The details of the GPS RO method and retrieval technique are provided by Kursinski et al. (1997). The estimated precision of COSMIC temperature measurements is 0.1% (Alexander et al., 2014). The root mean square difference in the temperature between radiosonde and COSMIC GPSRO is found around 0.64 K between 10 and 27 km (Rao et al., 2009). In the present study, we used Level 2 dry profiles from the COSMIC GPS RO data products at 2° x 2° spatial resolution.

2.6. CALIOP on-board CALIPSO satellite

For investigating the spatial distribution of the ATAL and its upper boundary, we used Cloud-Aerosol LIdar with Orthogonal Polarization (CALIOP) on-board Cloud-Aerosol Lidar and Infrared Pathfinder Observation (CALIPSO) (Winker et al., 2009) during 2014–2018 which operates at 532 nm. CALIOP is a nadir viewing, sun synchronised active remote sensing instrument with two optical wavelengths (1064 nm and 532 nm) produced simultaneously by the frequency doubling method. These lasers produce a peak power of 100 mJ at a pulse repetition rate of 20.16 Hz. Initially, we used the level 3 (L3) CALIOP extinction profile to illustrate the spatial distribution of the ATAL during the study period. Since the CALIOP L3 product does not provide aerosol information in the upper troposphere (<16 km) over the ASMA region, we used the level 1 (L1) CALIOP data product to obtain the backscatter ratio at 532 nm between 10 and 22 km. To overcome the low signal-to-noise ratio of the CALIOP observation in the UTLS region, Vernier et al. (2009, 2015,

2018) have developed a specific treatment for the level 1 product to retrieve the backscatter profiles in the UTLS region. The data sets used in the present study is obtained from the same algorithm at 5° x 2° (lon x lat) spatial resolution. In the present study, we didn't use CALOP observations after August 15, 2017 and 2019 to avoid the effect of smoke from the Canadian wildfire and Raikoke eruption, respectively.

2.7. ERA5 reanalysis

In the present study, we also used European Centre for Medium-Range Weather forecasts (ECMWF) Re-Analysis-5 (ERA-5) datasets. ERA-5 is the fifth generation of the ECMWF atmospheric reanalysis of the global climate data set with a higher time resolution than the previous version of ERA-Interim (Hersbach et al., 2020). We used ERA-5 temperature, zonal wind, and potential vorticity at 18:00 UTC at 1° x 1° spatial resolution at 37 pressure levels.

2.8. Identification of tropopause parameters and cloud removal using wavelet covariance transform (WCT)

In the present study, we used altitude profiles of temperature (T), potential temperature (θ) and square of Brunt-Väisälä frequency (N^2) from radiosonde observations over three locations to identify the different tropopause parameters such as cold point tropopause height (CPH), lapse rate tropopause height (LRH), the convective overflow height (COH) and the layer of maximum stability (LmaxS) by following Sunilkumar et al. (2017). The CPH and LRH are derived from temperature profiles. The coldest point in the temperature profile below 20 km is considered as CPH. The traditional WMO tropopause (LRH) is defined as 'the lowest level at which the lapse rate becomes less than 2 K/km, provided that the average lapse rate from this level to the next 2 km remains less than 2 K/km (WMO, 1957)'. The COH is identified from the minimum gradient of θ below CPH after smoothening the nine-point running mean (Gettelman and Forster, 2002). If there are multiple troughs, then whose value is less than 5 times the minimum value and is less than 5 K/km and close to the CPH is considered as COH (Mehta et al., 2008). The altitude at which the N^2 peaks is identified as the LmaxS (Gettelman and Wang, 2015; Sunilkumar et al., 2017) after smoothening nine-point running mean. N^2 is calculated from potential temperature derived from radiosonde observations and defined as $N^2 = \left(g/_{\theta}\right)\left(d\theta/_{dz}\right)$ where, g is the acceleration due to gravity and dz is the vertical interval. The maximum static stability is a result of the shape of the temperature profile. The thermal profile is a consequence of the radiative (Randel et al., 2007) and/or dynamical processes (Son and Polvani, 2007; Grise et al., 2010).

We performed Wavelet Covariance Transform (WCT) (Brooks, 2003; Pandit et al., 2014) analysis to detect cloud layers in the observed backscatter ratio profile. Once the cloud top and bottom are identified, the corresponding cloud layers are removed from the profile to create cloud-free backscatter ratio profiles. The WCT for the backscatter ratio profile is defined as,

$$W_p(a,b) = \frac{1}{a}\int_{z_b}^{z_t} P(z)\,h\left(\frac{z-b}{a}\right)dz \tag{1}$$

With the Haar function,

$$h\left(\frac{z-b}{a}\right) = \begin{cases} +1, b-\frac{a}{2} \le z \le b, \\ -1, b \le z \le b+\frac{a}{2} \\ 0, \textit{elsewhere} \end{cases} \tag{2}$$

P(z) in equation (1) is the backscatter signal from COBALD sonde, z is the altitude, z_b and z_t are the lower and upper limit of the profile, respectively. In the Haar function, b and a are called translation and dilation, respectively. An appropriate selection of a is the main challenge in accurate detection of the cloud layer. After going through different profiles and experimenting with various values, $a = n \times \Delta z = 200$ m is chosen with n = 8 and altitude resolution, $\Delta z = 25$ m. The dilation a is the extent of the step function, $h\left(\frac{z-b}{a}\right)$ and translation b determines the location of the step. Negative and positive peaks are used to identify the cloud base and top with respect to a pre-defined threshold value. An appropriate threshold for the detection of cloud is fixed after inspecting multiple profiles and further verified the cloud detection by checking manually. We fixed the threshold in such a way that the $BSR_{455} > 1.12$ (Hanumanthu et al., 2020) will be identified as a cloud layer around the UTLS (10–22 km) region. By making use of threshold values that linearly varies as a function of altitude it is possible to remove multiple clouds as well as, geometrically and optically thin clouds (Pandit et al., 2014) from the backscatter signal. However, the prior knowledge of the backscatter ratio that represents the cloud layer helps here to fix the threshold to a single value.

3. Results

3.1. Defining the top of the ATAL

In this study, we derived all the tropopause parameters from individual observations which have a minimum altitude coverage of 22 km. Fig. 2(a–c) shows the altitude profiles T, the gradient of θ (dθ/dz) and N^2 obtained from radiosonde observations on August 01, 2017,17:30 UTC over Gadanki, respectively. The tropopause parameters identified from these profiles are shown with labelled dash lines. The CPH is located around 17.0 km with a potential temperature (temperature) of 374.30 K (190.94 K). The LRH is found at 16.80 km, 200 m below the CPH with a potential temperature (temperature) of 370.86 K (191.12 K). The COH is located around 12.5 km and the potential temperature (temperature) is found to be 351.97 K (218.42 K). N^2 peaked around 18.4 km, 1.4 km above CPH and marked the LmaxS with a potential temperature (temperature) of 428.43 K (203.74 K). The simultaneous observation of the backscatter ratio at 455 nm (BSR_{455}) from the COBALD sonde is shown in Fig. 2(d) along with the tropopause parameters from the radiosonde. Two high-level clouds have been noticed around 11 km and 15.7 km with a thickness of 600 m and 250 m, respectively. An increase in BSR_{455} above the tropopause is noticeable and it shows a minimum around the LmaxS. The LmaxS coincide with a thermal inversion and this inversion limits the further vertical extend of the ATAL. Therefore, the top of the ATAL can be determined by the upper-level inversion, a few meters/kilometers above the tropopause. Fig. 3 shows individual profiles of BSR_{455} and T over Gadanki, Hyderabad and Varanasi along with tropopause parameters suggesting as well that LmaxS can be considered as the upper boundary of the ATAL. The mean BSR_{455} is estimated by removing the clouds from individual profiles using the wavelet covariance transform (WCT) method. The raw BSR_{455} profile, WCT corresponding to the raw BSR_{455} profile and cloud removed BSR_{455} on August 01, 2017, 17:30 UTC over Gadanki are assembled in Fig. S1. To avoid potential contamination, we have removed BSR_{455} of a few meters below and above the cloud layer. The mean BSR_{455} with tropopause parameters estimated from the corresponding radiosonde observations are shown in Fig. 4. The mean CPH over Gadanki, Hyderabad and Varanasi are found at around 16.75 ± 0.68 km, 17.08 ± 0.42 km and 17.33 ± 0.90 km, respectively with a potential temperature of 373.35 ± 10.45 K, 377.69 ± 5.65 and 378.95 ± 14 K, respectively. The mean LmaxS over these locations is seen around 18.98 ± 0.70 km, 18.84 ± 0.91 and 20.01 ± 1.0 km, respectively, with a potential temperature of 444.61 ± 20.81 K, 438.14 ± 27.43 and 450.18 ± 28.18 K, respectively. The LmaxS is found about 1.7–2.7 km above the CPH over these three locations during the monsoon season (June-July-August (JJA)). The BSR_{455} shows a minimum at LmaxS and this minimum separate the ATAL from the stratospheric aerosol layer (Junge layer).

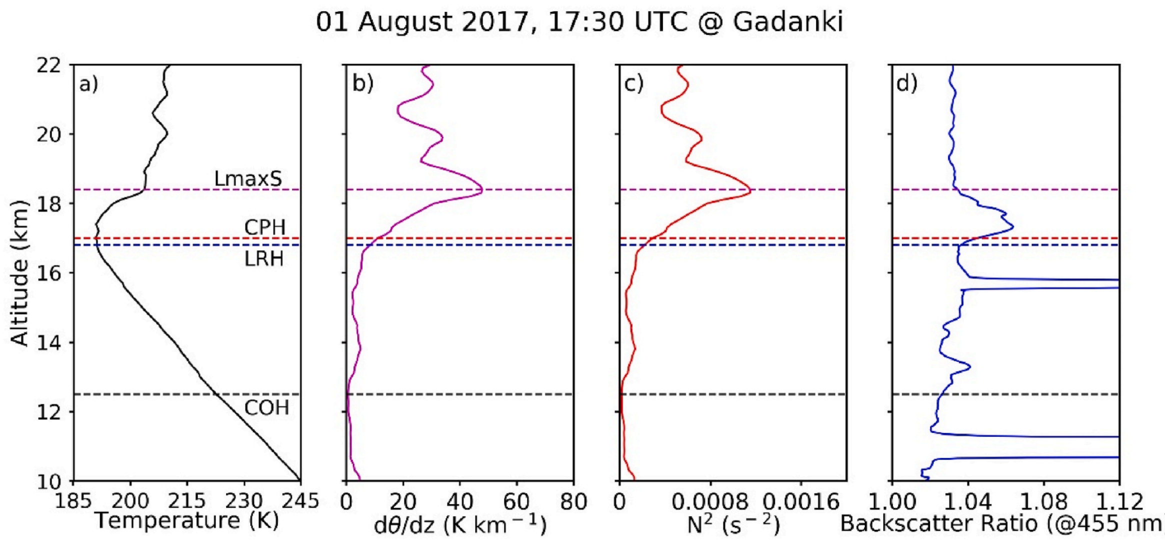

Fig. 2. Profiles of (a) temperature, (b) potential temperature gradient (dθ/dz) and (c) square of Brunt Väisäla frequency (N^2) derived from August 01, 2017, 17:30 UTC radiosonde measurement over Gadanki. (d) Profile of backscatter ratio at 455 nm observed during the same launch using a COBALD sonde. The solid dash lines indicate the tropopause parameters derived from the radiosonde observations and they are labelled in (a).

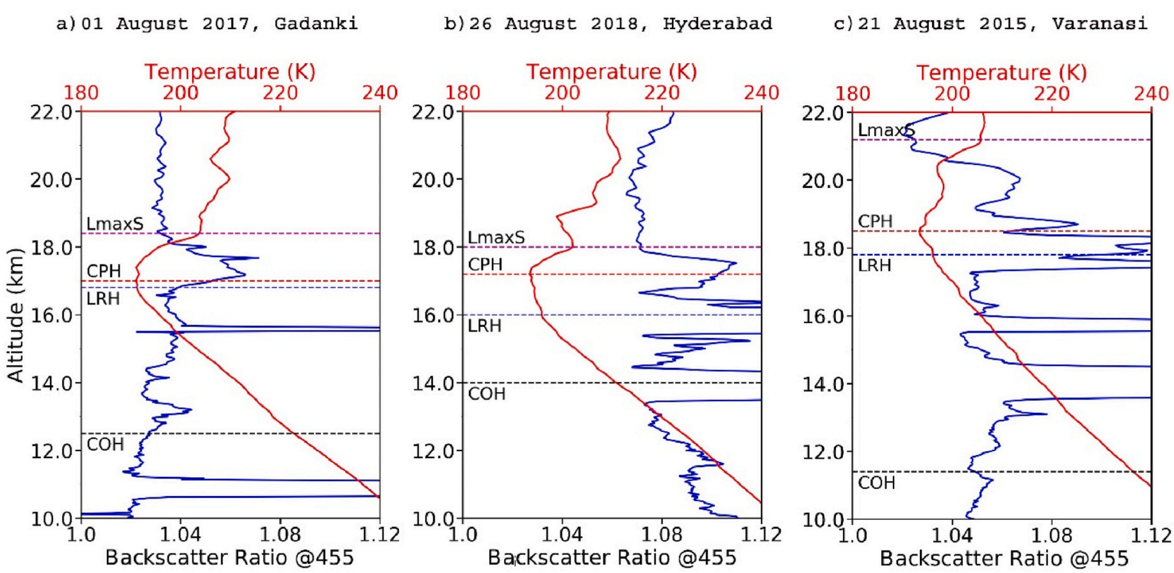

Fig. 3. Backscatter ratio at 455 nm and temperature profile over (a) Gadanki on August 01, 2017, (b) Hyderabad on August 26, 2018, and (c) Varanasi on August 21, 2015. The dashed lines indicate the respective day's tropopause parameters derived from radiosonde observations.

3.2. *Water vapor, ozone and cloud from balloon-borne observations*

Our analysis of water vapor and ozone from CFH and ozonesonde measurements reveals distinct features around the tropopause. Mean profiles of water vapor and ozone (8 profiles) from simultaneous CFH and ozonesonde measurements along with mean tropopause parameters calculated from individual observations over Hyderabad are shown in Fig. 5. A confined layer of water vapor is observed between CPH and LmaxS with a localised maximum of ~ 5ppmv in the mean profile. The two vertical dashed lines indicate 4 ppmv (blue) and 5 ppmv (red) of water vapor mixing ratio. The minimum water vapor mixing ratio (~4 ppmv) is observed around CPH and LmaxS (within the standard deviation). Mean CPH (θ) from these observations is found at around 17.20 ± 0.31 km (377.06 ± 4.66 K) and LmaxS(θ) is located around 18.37 ± 0.28 (423.00 ± 7.12 K). The ozone mixing ratio profile shows higher variability between COH and LRH and it shows a sharp increase in its concentration above LRH. However, the mean ozone profile shows a small variation around the LmaxS, and the ozone shows a steady increase above this stable layer. In Fig. S2 we have shown mean ozone profiles from all the available observations over Gadanki (14 profiles), Hyderabad (28 profiles) and Varanasi (3 profiles) along with the mean tropopause parameters estimated from individual profiles. The sharp gradient in the mean ozone profile around the LRH is clearly noticeable in all three station's observations. However, the change in the ozone concentration around the LmaxS is not prominent, though a small change is observed. In Figs. S3a and S3b, we plotted ozone relative difference and ozone mean absolute difference over Hyderabad along with tropopause parameters, respectively. The ozone relative difference is mostly less than 20 ppbv below COH and it gradually increases from COH to LmaxS and beyond. Variation in ozone mixing ratio near the tropopause and LamxS is clearly depicted in the mean ozone absolute difference than in the ozone relative difference profiles. The higher gradient in mean ozone absolute difference coincides with the COH, LRH/CPH and LmaxS (within the standard deviations). High altitude

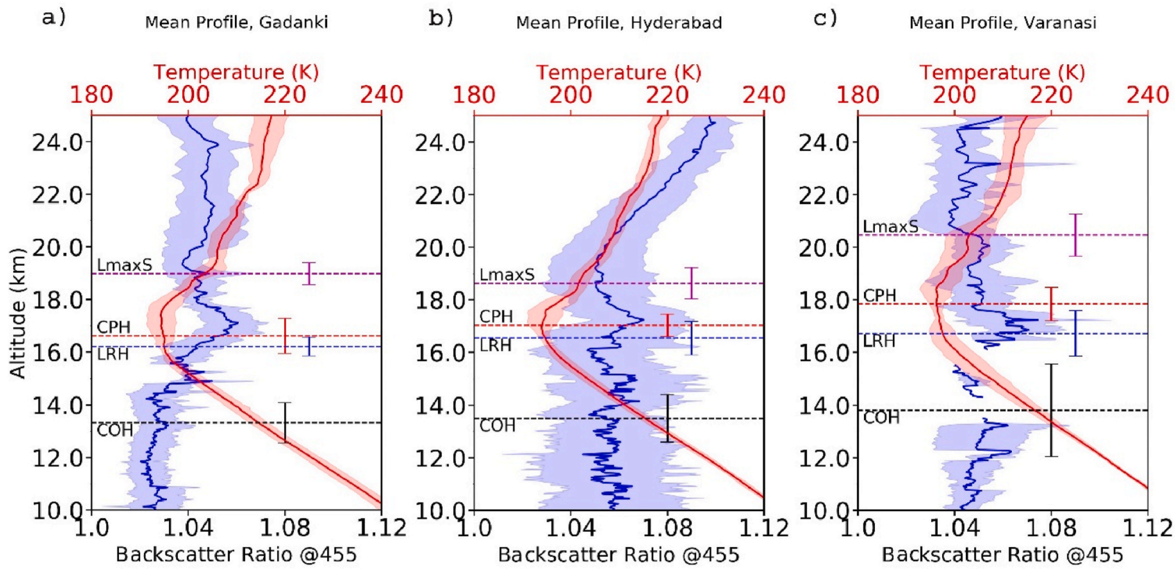

Fig. 4. Cloud removed mean backscatter ratio at 455 nm (blue) and mean temperature (red) along with their standard deviation observed over (a) Gadanki (6 profiles), (b) Hyderabad (11 profiles) and (c) Varanasi (6 profiles). The dashed straight lines show the mean tropopause parameters and its standard deviations are indicated with vertical bars.

clouds were being detected by COBALD sonde during the BATAL campaign. Convection frequently reaches the tropopause height during the Asian Summer Monsoon (ASM) (Basha et al., 2021), not necessarily penetrating the tropopause, however. The overshooting clouds can hydrate the lower stratosphere by injecting ice crystals directly into the lower stratosphere (~420 K) (Corti et al., 2008). Our observation on August 17, 2018, 19:40 UTC using COBALD and CFH sondes detected an overshooting cloud with cloud top (~385.22 K) above CPH (~374.64 K) and shown in Fig. 5(c). The BSR_{455} (>1.12) and RH_{ice} (>78%, >12 km) (Narendra Reddy et al., 2018; Renju et al., 2021) clearly show a cloud extending from 15.5 km–17.6 km (~364.01 K–385.22 K). The approximate temperature at which all the liquid water will spontaneously condense into ice crystals is −40 °C (Pruppacher and Klett, 1980; Koop et al., 2000). The observed clouds base was found around 15.5 km with a temperature of −73.3 °C and hence it is an ice cloud. On that day, the CPH and LRH were found to be at the same altitude, ~17.2 km with a minimum water vapor mixing ratio of ~3.40 ppmv. Above cloud top, an enhancement in water vapor with a maximum of ~5.68 ppmv (RH_{ice}, ~60%) is noticed, and the concentration decreases to typical stratospheric value around the LmaxS. An enlarged view of the tropopause region is shown in Fig. 5(d) along with tropopause parameters to portray the enhanced water vapor layer above the cloud top. Though the increase in the water vapor is small, it is significant in the tropical lower stratosphere at cold temperatures. Higher water vapor at this cold temperature can favour the in-situ production of aerosols via photochemistry (Höpfner et al., 2019) as well as the hygroscopic growth of the aerosols in the UTLS region (He et al., 2019). Simultaneously observed ozone from ozonesonde recorded low concentration in the upper troposphere and started to increase around CPH/LRH. The ozone profile has also shown a variation in its concentration around LmaxS, however, the change was small. A similar overshooting cloud is also detected over Nainital, India during 2016 balloon-borne observations using COBALD and CFH sondes (Hanumanthu et al., 2020, Fig. 2 and Fig. A1, 12-08-2016).

In addition to this, we also noticed an enhancement in water vapor below the tropopause, ~16 km and around COH in the mean water vapor profile (Fig. 5(a)). This enhancement in water vapor may be according to the hypothesis by Schoeberl et al. (2019). Most of the convection detrained around the COH and are the primary source of water vapor in the tropical tropopause layer (TTL), region between COH and CPH. Within TTL, the water vapor slowly ascends within the anticyclone and increases the RH_{ice} with altitude. Once the RH_{ice} reaches the cloud nucleation level, ice crystals start to form in the upper TTL region. They fall through the TTL and grow in the saturation region by dehydrating the TTL and eventually sublimate below the TTL and hydrate the lower boundary of the TTL. This repetitive process enhances water vapor below the tropopause and around the COH, as observed. Higher RH_{ice} values near the COH and around the CPH are prominent in Fig. 5(d). Above the tropopause, the RH_{ice} decreases since the temperature starts to rise in the lower stratosphere. The meteorological condition on August 17, 2018 is provided in Fig. S4. Higher tropopause over the monsoon region is noticed on August 17, 2018 compare to the global mean tropopause. PV anomaly shows higher PV on this day between sub-tropical jet (thick black line) and tropical easterly jet streams (thick dashed black line) (20–40° N) near the tropopause.

3.3. Aerosols from the satellite observations

ATAL is seen in both in-situ and satellite observations around the cold point tropopause region. Stratospheric aerosol extinction from CALIOP is shown in Fig. S5 over the Indian region (65–110° E) and a high extinction coefficient is observed around the ATAL region. The extinction coefficient shows the presence of ATAL well above the CPH and minimum near LmaxS. However, the level 3 (L3) CALIOP extinction profile does not provide aerosol information in the upper troposphere (~10–16 km). To overcome this limitation, we used the CALIOP L1 data product with a specific treatment (Vernier et al., 2009, 2015, 2018). The zonal (65–110° E, Indian region) and meridional (15–25° N) average cloud-free aerosol backscatter ratio at 532 nm (BSR_{532}) from CALIOP is shown in Fig. 6(a) and (b), respectively. The ATAL is located above 5° N latitude belt with maximum BSR_{532} between ~15 and 27.5° N. The average meridional BSR_{532} shows the ATAL between 0° – 150° E with maximum aerosols between 15 and 120° E. Similarly, higher BSR is seen around CPH, and above CPH the BSR_{532} gradually decreases with the altitude and forms a layer of low BSR_{532}. This low BSR_{532} layer matches with the COSMIC GPSRO derived LmaxS (within the standard deviation). The BSR start to increase gradually above the LmaxS and it identifies the stratospheric aerosol layer called ‘Junge Layer’. The gradual decrease and attaining a low BSR around LmaxS above CPH is clearly noticed in both the COBALD and CALIOP observations.

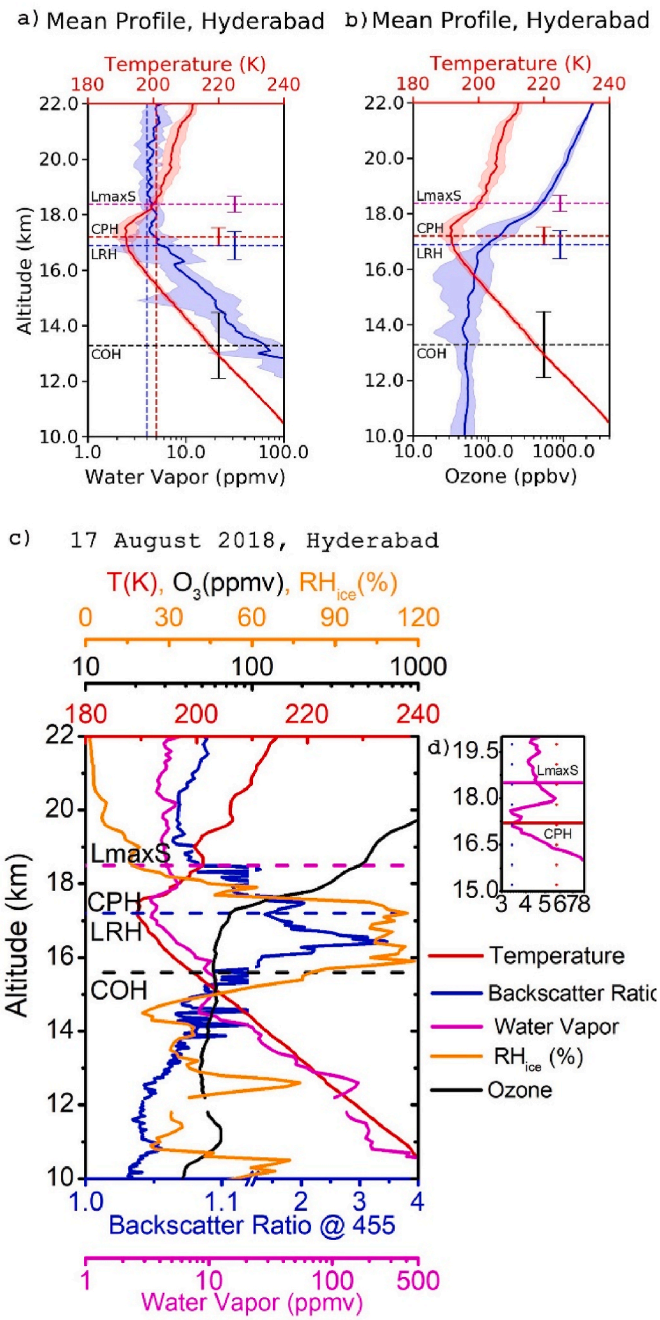

Fig. 5. Profiles of (a) mean water vapor mixing ratio and (b) ozone mixing ratio along with mean temperature profile over Hyderabad. The blue and red shades show the standard deviation of the observations. The dashed straight lines in figure (a) and (b) indicates the mean tropopause parameters and the vertical bars show their standard deviation. (c) The simultaneously observed backscatter ratio at 455 nm (blue), water vapor mixing ratio (magenta), ozone mixing ratio (black), temperature (red) and relative humidity over ice (orange) on August 17, 2018 over Hyderabad. The dashed straight lines indicate the tropopause parameters derived from the radiosonde observations and are labelled accordingly. An enlarged view of the water profile is shown in (d) along with tropopause parameters. The dotted vertical line in the enlarged plot corresponds to the water vapor mixing ratio of ~3.40 ppmv (blue) and ~5.68 ppmv (red).

Therefore, the lower stratospheric temperature inversion act as a capping inversion for the ATAL and it restricts the further upward transport of aerosols by the weak BDC during NH monsoon.

We have utilized the COSMIC-GPSRO satellite dry profiles to

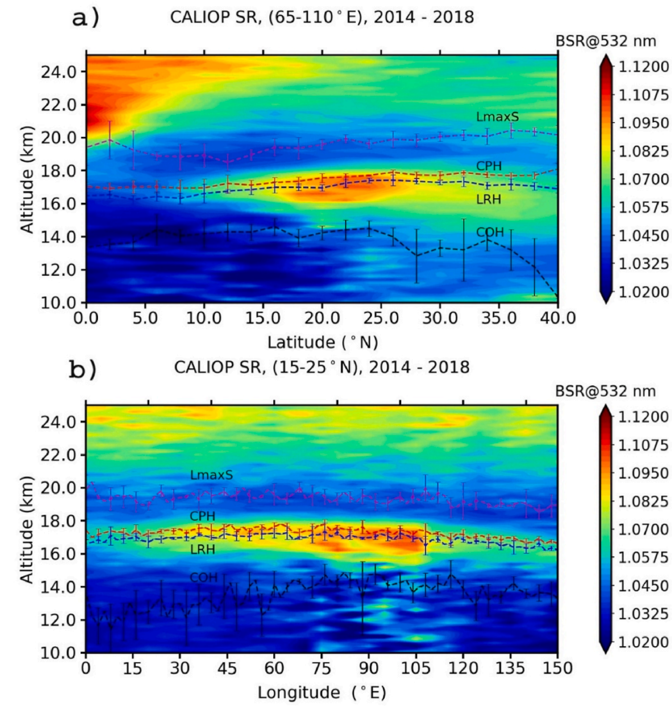

Fig. 6. (a) The zonal mean (65–110° E) and meridional mean (15–25° N) backscatter ratio at 532 nm from CALIOP observation during 2014–2018 as a function of altitude. The dashed straight lines with vertical bars indicate the mean and standard deviation of the tropopause parameters derived from COSMIC GPS-RO satellite's dry temperature and pressure profiles during the same period and they are labelled in the figures.

calculate the tropopause parameter within the anticyclone. The mean CPH (θ) within the anticyclone is around 17.50 ± 0.29 km (392.30 ± 6.27 K). The LRH(θ) is found at around 17.00 ± 0.25 km (383.84 ± 4.72 K). The minimum potential temperature gradient is located around 13.10 ± 0.96 km with a θ of 355.78 ± 5.18 K. The LmaxS(θ) is found around 19.63 ± 0.46 km (454.39 ± 13.89 K) within the anticyclone.

4. Summary and discussion

The existence of the lower stratospheric aerosol layer known as 'Junge Layer' and the elevated upper tropospheric aerosol layer called ATAL are well established. However, what separates these two layers was not yet clear so far since the ATAL is observed well above the tropopause. In this study, we introduced the concept of static stability (LmaxS) to define the top of the ATAL. The LmaxS derived from radiosonde along with the backscatter ratio from COBALD sonde observations has clearly shown that the ATAL can vertically extend up to the LmaxS and beyond that, the Junge layer exists. This has been verified using balloon measurements from multiple locations over India and the satellite observations provided a similar but a regional picture. Now, we will further discuss how the LmaxS is acting as an upper boundary for the ATAL with the observed results and in light of the other supporting information.

The higher water vapor mixing ratio found near the cold point tropopause suggests deep convection can reach up to the upper troposphere and even penetrate the tropopause, which could also transport other trace gases, aerosols or its gas phase precursors (Fig. 5(a)). The water vapor peak between CPH and LmaxS is consistent with the hydration of the lower stratosphere by overshooting convective uplifts/anvils (Fig. 5(c)). Our balloon observations of overshooting cloud, higher water vapor above CPH and ATAL around tropopause are consistent with the earlier studies. In-situ observations from both balloon-borne and aircraft measurements have shown clear evidence of direct transport of ice particles and water vapor into the lower stratosphere (Corti et al., 2008; Lee et al., 2019; Khaykin et al., 2021). The Geophysica campaign observations by Corti et al. (2008) has shown convective system penetrated the stratosphere and deposits of ice particle at altitude reaching 420 K potential temperature. In the present study, we have observed a cloud top reaching an altitude (17.6 km) corresponding to 386.98 K potential temperature and above this level, evaporation of ice crystal leads to an increase in vapor (Fig. 5(d)). The top of the enhanced water vapor layer matches with the LmaxS at a potential temperature 425.5 K. The hydration of the lower stratosphere by direct injection of ice crystal and later evaporation provides favourable conditions for new particle formation at low temperature and pressure in the presence of sunlight (Vernier et al., 2018; Höpfner et al., 2019 and references therein). Apart from this, the higher water vapor also facilitates hygroscopic growth of aerosols which are convectively transported as well as in-situ generated in the UTLS (He et al., 2019). Various model simulations have reported that the sulphur dioxide (SO_2), the sulphate aerosol precursors, can survive the convective uplift and reach up to the UTLS. The ammonia (NH_3) observations from the MIPAS satellite and AN observations from the CRISTA (Höpfner et al., 2019) also agree with the hypothesis of new particle formation at UTLS.

Our analysis suggests that the LmaxS found ~1 km–2.7 km above the CPH corresponding to the potential temperature ~442.11 ± 25.64 K (454.39 ± 13.89 K) over India (ASMA) marks the upper boundary of the ATAL. The balloon observations over India show a mean BSR_{455} of ~1.048 ± 0.016 at LmaxS, ~19.27 ± 0.87. The BSR_{455} observations from CALIOP over the ASMA region also show that the LmaxS identify the top of the ATAL with a BSR value of ~1.045 and above the LmaxS the BSR once again starts to increase with the altitude and it marks the Junge layer. The concept of an upward spiral region within the ASMA with its upper boundary around 460 K potential temperature (Vogel et al., 2019) is in good agreement with our LmaxS. The mean altitude (potential temperature) of LmaxS is located over Gadanki, Hyderabad and Varanasi at 18.98 ± 0.70 km (444.61 ± 20.81 K), 18.84 ± 0.91 km (438.14 ± 27.43 K) and 20.01 ± 1.00 km (450.18 ± 28.18 K), respectively. The LmaxS limit the ATAL, possibly because it is mainly composed of small liquid aerosols (~80% - 95%) formed from gas to liquid conversion via photochemistry at low temperature and pressure in the presence of higher water vapor around the CPH (Vernier et al., 2018). The existence of a higher water vapor mixing ratio above the CPH also implies the same. Further, these higher water vapor concentrations could trigger the hygroscopic growth of the liquid or solid aerosols formed in-situ in the UTLS and the aerosols transported to the upper troposphere via deep convection over south Asia (He et al., 2019). This will also limit the upward transport of aerosols via weak Brewer-Dobson Circulation (BDC) during the northern hemisphere monsoon along with the temperature inversion at LmaxS. Therefore, a part of the aerosols may sediment back to the upper troposphere under the action of gravity and limits its increase in the concentration in the lower stratosphere alike the water vapor freeze-drying and ice crystal formation at tropical tropopause. The large scale BDC transports the pollutants to a higher altitude above 460 K via the tropical pipe (within ~1 year) (Vogel et al., 2019).

The observed changes in ozone in between the CPH and LmaxS is due to the injection of tropospheric air into the lower stratosphere. However, the strong gradient in ozone mixing ratio observed around the lapse rate tropopause suggests almost all updraft becomes weaker around LRH and further uplift by spiralling range take a few days. The mean tropopause parameters and their corresponding potential temperature is provided in Table 2. The bottom layer of the proposed spiralling range (~360 K) by Vogel et al. (2019) is found between the COH and LRH. We also analysed ACE- FTS satellite trace gas products such as CO, H_2O, HCN and O_3 to further verify the role of LmaxS in defining the upper boundary of the ATAL and ASMA and shown in Fig. 7. It is clear from the figure that there is no sharp gradient exists in any of these trace gases around the LRH or CPH. The tropospheric traces gases such as CO, H_2O and HCN shows high mixing ratio in the upper troposphere and its mixing ratio decreases with altitude and reaches a typical stratospheric background value around LmaxS. The CPH and LRH locate well below the level of typical stratospheric background mixing ratio and this indicates significant stratospheric in-mixing, which further implies neither CPH nor the LRH represents the separation between the troposphere and stratosphere in the ASMA region in both chemical and dynamical sense. Thus, the 'tropospheric bubble' (Pan et al., 2016) not only extends to the exceptionally high tropopause but also to the lower stratosphere over ASMA. The carbon monoxide and ozone relationship for the ATAL and pacific (0–40° N, 180° W- 140° W) regions during 2014–2018 are shown in Fig. S6 with corresponding potential temperatures (colored open circles). In the scatter plot, the filled diamond scatters show the CPH (red border) and LmaxS (black) potential temperatures, and the filled square boxes show COH (red) and LRH (black) potential temperatures, respectively. The transition of the trace gas mixing ratio in the UTLS region is well represented in the CO–O_3 tracer -tracer famous 'L' shape curve. CO mixing ratio shows a gradual reduction from its higher values around COH altitude, where almost all convection ceases and from the same altitude O_3 mixing ratio started to increase. As we showed in Fig. 7, the CO mixing ratio approaches its stratospheric background mixing ratio around LmaxS and O_3 shows a steady increase in its mixing ratio above LmaxS. However, the 'L' isn't as sharp as in other regions such as the extra-tropics and the smoother transition between the tropospheric and stratospheric branches could be an indication of a transition or missing layer. The observed higher mixing ratio of trace gases above tropopause and approaching the mixing ratio to the typical stratospheric background value is in good agreement with the recent aircraft observations by Hobe et al. (2021). However, the poor vertical resolution of ACE-FTS is inadequate to explain the possible photochemical loss of trace gases such as CO and define the top of the ASMA as LmaxS. High vertical resolution in-situ observations and model outputs are required to investigate the role of LmaxS as the top of ASMA since not only the microphysical properties limit the transport of the trace gases to the lower stratosphere but also the photochemical reactions.

Table 2
Average tropopause parameters estimated over Gadanki, Hyderabad and Varanasi from radiosonde measurements during the 2014–2019 BATAL campaigns.

	Gadanki		Hyderabad		Varanasi	
	km	Θ (K)	km	Θ (K)	km	Θ (K)
CPH	16.75 ± 0.68	373.35 ± 10.45	17.08 ± 0.42	377.49 ± 5.65	17.325 ± 0.90	378.95 ± 14.04
LRH	16.26 ± 0.43	366.69 ± 4.67	16.62 ± 0.59	371.49 ± 6.49	16.5 ± 0.81	367.80 ± 4.10
COH	13.05 ± 1.10	352.02 ± 3.47	13.30 ± 1.18	354.92 ± 4.20	13.92 ± 1.69	358.71 ± 2.86
LmaxS	18.98 ± 0.70	444.61 ± 20.81	18.84 ± 0.91	438.14 ± 27.43	20.01 ± 1.00	450.18 ± 28.18

5. Conclusions

We analysed balloon measurements of aerosol backscatter ratio, ozone, water vapor, temperature and tropopause parameters over Gadanki, Hyderabad and Varanasi conducted during 2014–2019 as a part of Balloon Measurement Campaigns of the Asian Tropopause Aerosol Layer (BATAL) to identify the top of the ATAL. We also make use of multi-satellite observations to investigate its spatial behaviour. The main conclusions drawn from the study are listed below.

1. Our balloon-borne observations over India and CALIOP and COSMIC GPSRO observations over Asian Summer Monsoon Anticyclone (ASMA) region suggest that the layer of maximum stability (LmaxS) derived from the square of Brunt Väisäla frequency (N^2) can define as the top of the Asian Tropopause Aerosol Layer (ATAL) and it separates the ATAL from the well-known stratospheric 'Junge layer'.

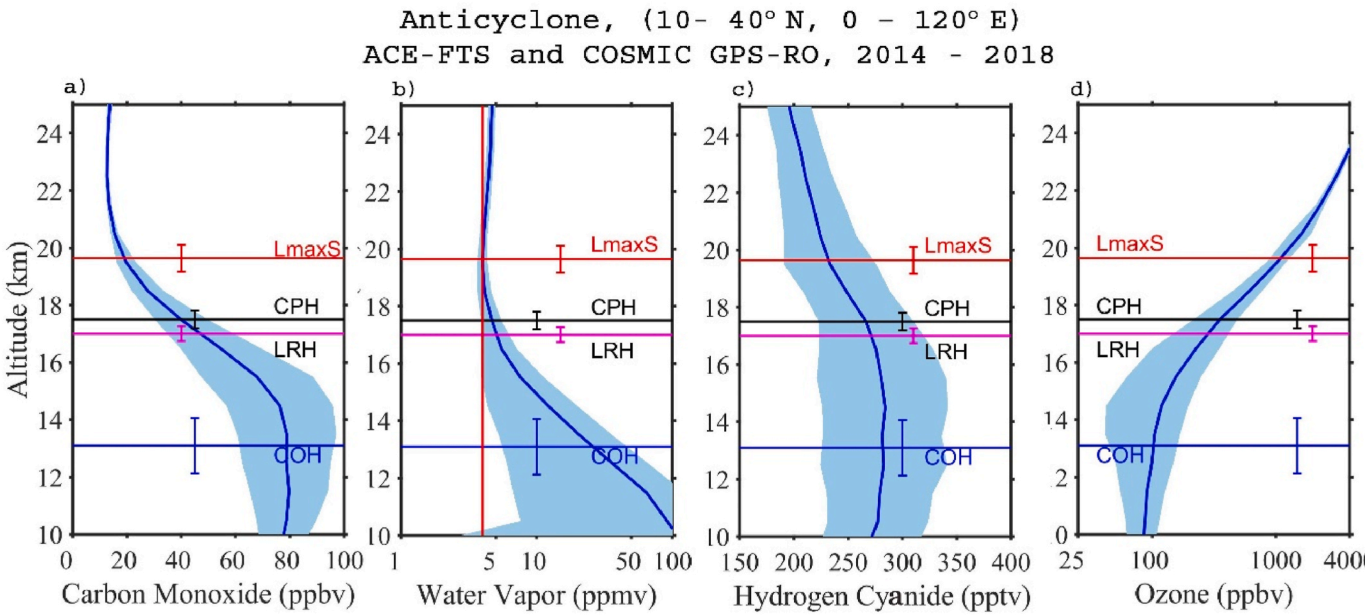

Fig. 7. The average profile of (a) carbon monoxide (CO), (b) Water Vapor (H_2O), (c) Hydrogen Cyanide and (d) ozone inside the anticyclone (10–40° N, 0–120° E) during 2014–2018. The straight lines indicate the mean tropopause parameters inside the anticyclone during the same period derived from the COSMIC GPS-RO dry temperature and pressure profiles. The vertical bar in the figures indicates the standard deviation of the tropopause parameters. The res vertical line in (b) represents 4 ppmv.

2. The LmaxS is found 1–2.7 km above the cold point tropopause corresponding to the potential temperature ~442.11 ± 25.64 K (454.39 ± 13.89 K) over India (ASMA) and the COBALD observations over Indian stations show that the typical value of BSR_{455} at LmaxS is ~1.048 ± 0.016.
3. The top of the enhanced water vapor layer in the lower stratosphere also coincides with the LmaxS with a secondary minimum in its concentration.
4. The trace gas observations from the ACE-FTS satellite do not show a sharp gradient in its concentration around tropopause. A gradual reduction in tropospheric trace gas concentration is observed above the CPH and it approaches the stratospheric background value around LmaxS. However, without considering the photochemical processes and mixing within the ASMA region during the slow ascent of air masses we could not conclude whether the LmaxS can also consider as the top of the ASMA tropospheric bubble.

Trace gases are not affected by microphysics while crossing the tropopause region. Hence, the photochemical reaction and lifespan of a trace gas are required to define the upper boundary of the confined ASMA region. The ACE-FTS observations show no sharp gradient in trace gas concentration and a gradual reduction in its concentration. Therefore, high vertical resolution in-situ observations and model simulation are required to verify further whether the LmaxS can consider as the top of the confined ASMA region or ASMA tropospheric bubble.

CRediT authorship contribution statement

S.T. Akhil Raj: Methodology, Visualization, Data curation, Writing – original draft. **M. Venkat Ratnam:** Visualization, Resources, Supervision, Writing – review & editing. **J.P. Vernier:** Resources, Data analysis, Writing – review & editing. **A.K. Pandit:** Writing – review & editing. **Frank G. Wienhold:** Data curation, Writing – review & editing.

Declaration of competing interest

The authors declare that they have no known competing financial interests or personal relationships that could have appeared to influence the work reported in this paper.

Acknowledgements

The results presented in this paper are obtained from the ISRO-NASA joint BATAL campaign supported by the National Atmospheric Research Laboratory (NARL), Department of Space (DoS) and NASA ROSES Upper Atmospheric Research and Atmospheric Composition Modelling and Analysis programs (UARP, ACMAP). We would like to thank technicians and engineers from NARL, TIFR Balloon Facility and BHU Varanasi for their help during the BATAL campaigns. We would like to thank Dr. T. D. Fairlie and Prof. A. Jayaraman for their initial helps in the realization of this project. The authors acknowledge UCAR/CDAAC and the ACE satellite mission funded by the Canadian Space Agency for providing COSMIC GPSRO and ACE-FTS data sets through their websites, respectively. We also thank CALIPSO, satellite teams for providing data sets through their website. We also thank Giovanni (https://giovanni.gsfc.nasa.gov/giovanni/) for providing AIRS tropopause data through their website. We also like to thank the European Centre for Medium-Range Weather Forecasts ERA5 teams for providing the datasets through their website. Author Akhil Raj S T would like to thank Ms. Renju Nandan for the help related to the WCT analysis.

Appendix A. Supplementary data

Supplementary data to this article can be found online at https://doi.org/10.1016/j.apr.2022.101451.

References

Akhil Raj, S.T., Venkat Ratnam, M., Narayana Rao, D., Krishna Murthy, B.V., 2015. Vertical distribution of ozone over a tropical station: seasonal variation and comparison with satellite (MLS, SABER) and ERA-Interim products. Atmos. Environ. 116, 281–292. https://doi.org/10.1016/j.atmosenv.2015.06.047.

Alexander, P., de la Torre, A., Llamedo, P., Hierro, R., 2014. Precision estimation in temperature and refractivity profiles retrieved by GPS radio occultations. J. Geophys. Res. 119, 8624–8638. https://doi.org/10.1002/2013JD021016.

Basha, G., Ratnam, M.V., Kishore, P., 2020. Asian summer monsoon anticyclone: trends and variability. Atmos. Chem. Phys. 20, 6789–6801. https://doi.org/10.5194/acp-20-6789-2020.

Basha, G., Ratnam, M.V., Jiang, J.H., Kishore, P., Babu, S.R., 2021. Influence of indian summer monsoon on tropopause, trace gases and aerosols in asian summer monsoon anticyclone observed by cosmic, mls and calipso. Rem. Sens. 13, 3984–4003. https://doi.org/10.3390/rs13173486.

Bernath, P.F., McElroy, C.T., Abrams, M.C., Boone, C.D., Butler, M., Camy-Peyret, C., Carleer, M., Clerbaux, C., Coheur, P.F., Colin, R., DeCola, P., DeMazière, M., Drummond, J.R., Dufour, D., Evans, W.F.J., Fast, H., Fussen, D., Gilbert, K., Jennings, D.E., Llewellyn, E.J., Lowe, R.P., Mahieu, E., McConnell, J.C., McHugh, M., McLeod, S.D., Michaud, R., Midwinter, C., Nassar, R., Nichitiu, F., Nowlan, C., Rinsland, C.P., Rochon, Y.J., Rowlands, N., Semeniuk, K., Simon, P., Skelton, R., Sloan, J.J., Soucy, M.A., Strong, K., Tremblay, P., Turnbull, D., Walker, K.A., Walkty, I., Wardle, D.A., Wehrle, V., Zander, R., Zou, J., 2005. Atmospheric chemistry experiment (ACE): mission overview. Geophys. Res. Lett. https://doi.org/10.1029/2005GL022386.

Bian, J., Li, D., Bai, Z., Li, Q., Lyu, D., Zhou, X., 2020. Transport of Asian surface pollutants to the global stratosphere from the Tibetan Plateau region during the Asian summer monsoon. Natl. Sci. Rev. 7, 516–533. https://doi.org/10.1093/nsr/nwaa005.

Birner, T., Dörnbrack, A., Schumann, U., 2002. How sharp is the tropopause at midlatitudes? Geophys. Res. Lett. 29, 1–4. https://doi.org/10.1029/2002GL015142.

Boone, C.D., Nassar, R., Walker, K.A., Rochon, Y., McLeod, S.D., Rinsland, C.P., Bernath, P.F., 2005. Retrievals for the atmospheric chemistry experiment Fourier-transform spectrometer. Appl. Opt. 44, 7218–7231. https://doi.org/10.1364/AO.44.007218.

Brunamonti, S., Jorge, T., Oelsner, P., Hanumanthu, S., Singh, B.B., Ravi Kumar, K., Sonbawne, S., Meier, S., Singh, D., Wienhold, F.G., Ping Luo, B., Boettcher, M., Poltera, Y., Jauhiainen, H., Kayastha, R., Karmacharya, J., DIrksen, R., Naja, M., Rex, M., Fadnavis, S., Peter, T., 2018. Balloon-borne measurements of temperature, water vapor, ozone and aerosol backscatter on the southern slopes of the Himalayas during StratoClim 2016-2017. Atmos. Chem. Phys. 18, 15937–15957. https://doi.org/10.5194/acp-18-15937-2018.

Corti, T., Luo, B.P., de Reus, M., Brunner, D., Cairo, F., Mahoney, M.J., Martucci, G., Matthey, R., Mitev, V., dos Santos, F.H., Schiller, C., Shur, G., Sitnikov, N.M., Spelten, N., Vössing, H.J., Borrmann, S., Peter, T., 2008. Unprecedented evidence for deep convection hydrating the tropical stratosphere. Geophys. Res. Lett. 35, 1–5. https://doi.org/10.1029/2008GL033641.

Fadnavis, S., Roy, C., Chattopadhyay, R., Sioris, C.E., Rap, A., Müller, R., Ravi Kumar, K., Krishnan, R., 2018. Transport of trace gases via eddy shedding from the Asian summer monsoon anticyclone and associated impacts on ozone heating rates. Atmos. Chem. Phys. 18, 11493–11506. https://doi.org/10.5194/acp-18-11493-2018.

Garny, H., Randel, W.J., 2016. Transport pathways from the Asian monsoon anticyclone to the stratosphere. Atmos. Chem. Phys. 16, 2703–2718. https://doi.org/10.5194/acp-16-2703-2016.

Gettelman, A., Forster, P.M. de F., 2002. A climatology of the tropical tropopause layer. J. Meteorol. Soc. Japan 80, 911–924. https://doi.org/10.2151/jmsj.80.911.

Gettelman, A., Wang, T., 2015. Structural diagnostics of the tropopause inversion layer and its evolution. J. Geophys. Res. 120, 46–62. https://doi.org/10.1002/2014JD021846.

Goff, J.A., Gratch, S., 1946. Low-pressure properties of water from -160 to 212. F. Trans. Amer. Soc. Heat Vent. Eng 52, 95–122.

Grise, K.M., Thompson, D.W.J., Birner, T., 2010. A global survey of static stability in the stratosphere and upper troposphere. J. Clim. 23, 2275–2292. https://doi.org/10.1175/2009JCLI3369.1.

Gu, Y., Liao, H., Bian, J., 2016. Summertime nitrate aerosol in the upper troposphere and lower stratosphere over the Tibetan Plateau and the South Asian summer monsoon region. Atmos. Chem. Phys. 16, 6641–6663. https://doi.org/10.5194/acp-16-6641-2016.

Hanumanthu, S., Vogel, B., Müller, R., Brunamonti, S., Fadnavis, S., Li, D., Ölsner, P., Naja, M., Singh, B.B., Kumar, K.R., Sonbawne, S., Jauhiainen, H., Vömel, H., Luo, B., Jorge, T., Wienhold, F.G., Dirkson, R., Peter, T., 2020. Strong day-to-day variability of the asian tropopause aerosol layer (ATAL) in August 2016 at the himalayan foothills. Atmos. Chem. Phys. 20, 14273–14302. https://doi.org/10.5194/acp-20-14273-2020.

He, Q., Ma, J., Zheng, X., Yan, X., Vömel, H., Wienhold, F.G., Gao, W., Liu, D., Shi, G., Cheng, T., 2019. Observational evidence of particle hygroscopic growth in the upper troposphere-lower stratosphere (UTLS) over the Tibetan Plateau. Atmos. Chem. Phys. 19, 8399–8406. https://doi.org/10.5194/acp-19-8399-2019.

He, Q., Ma, J., Zheng, X., Wang, Y., Wang, Y., Mu, H., Cheng, T., He, R., Huang, G., Liu, D., Lelieveld, J., 2020. Formation and dissipation dynamics of the Asian tropopause aerosol layer. Environ. Res. Lett. 16 https://doi.org/10.1088/1748-9326/abcd5d.

Hemanth Kumar, A., Ratnam, M.V., 2021. Variability in the UTLS chemical composition during different modes of the asian summer monsoon anti-cyclone. Atmos. Res. 260, 105700. https://doi.org/10.1016/j.atmosres.2021.105700.

Hersbach, H., Bell, B., Berrisford, P., Hirahara, S., Horányi, A., Muñoz-Sabater, J., Nicolas, J., Peubey, C., Radu, R., Schepers, D., Simmons, A., Soci, C., Abdalla, S., Abellan, X., Balsamo, G., Bechtold, P., Biavati, G., Bidlot, J., Bonavita, M., De Chiara, G., Dahlgren, P., Dee, D., Diamantakis, M., Dragani, R., Flemming, J., Forbes, R., Fuentes, M., Geer, A., Haimberger, L., Healy, S., Hogan, R.J., Hólm, E., Janisková, M., Keeley, S., Laloyaux, P., Lopez, P., Lupu, C., Radnoti, G., de Rosnay, P., Rozum, I., Vamborg, F., Villaume, S., Thépaut, J.N., 2020. The ERA5 global reanalysis. Q. J. R. Meteorol. Soc. 146, 1999–2049. https://doi.org/10.1002/qj.3803.

Hobe, M. Von, Ploeger, F., Konopka, P., Kloss, C., Ulanowski, A., Yushkov, V., Ravegnani, F., Volk, C.M., Pan, L.L., Honomichl, S.B., Tilmes, S., Kinnison, D.E., Garcia, R.R., Wright, J.S., 2021. Upward transport into and within the Asian monsoon anticyclone as inferred from StratoClim trace gas observations, pp. 1267–1285.

Höpfner, M., Ungermann, J., Borrmann, S., Wagner, R., Spang, R., Riese, M., Stiller, G., Appel, O., Batenburg, A.M., Bucci, S., Cairo, F., Dragoneas, A., Friedl-Vallon, F., Hünig, A., Johansson, S., Krasauskas, L., Legras, B., Leisner, T., Mahnke, C., Möhler, O., Molleker, S., Müller, R., Neubert, T., Orphal, J., Preusse, P., Rex, M., Saathoff, H., Stroh, F., Weigel, R., Wohltmann, I., 2019. Ammonium nitrate particles formed in upper troposphere from ground ammonia sources during Asian monsoons. Nat. Geosci. 12, 608–612. https://doi.org/10.1038/s41561-019-0385-8.

Hoskins, B.J., Rodwell, M.J., 1995. A model of the asian summer monsoon. Part I: the global scale. J. Atmos. Sci. 52, 1329–1340.

Khaykin, S.M., Moyer, E., Krämer, M., Clouser, B., Bucci, S., Lykov, A., Afchine, A., Cairo, F., Formanyuk, I., Mitev, V., Rolf, C., Singer, C., Spelten, N., Volkov, V., Yushkov, V., 2021. Persistence of moist plumes from overshooting convection in the Asian monsoon anticyclone. Atmos. Chem. Phys. Discuss. 1–27.

Kim, Y.-S., Shibata, T., Iwasaka, Y., Shi, G., Zhou, X., Tamura, K., Ohashi, T., 2003. Enhancement of aerosols near the cold tropopause in summer over Tibetan Plateau: lidar and balloonborne measurements in 1999 at Lhasa, Tibet, China. Lidar Remote Sens. Ind. Environ. Monit. III 4893, 496. https://doi.org/10.1117/12.466090.

Komhyr, W.D., Barnes, R.A., Brothers, G.B., Lathrop, J.A., Opperman, D.P., 1995. Electrochemical concentration cell ozonesonde performance evaluation during STOIC 1989. J. Geophys. Res. 100, 9231–9244. https://doi.org/10.1029/94JD02175.

Koop, T., Luo, B., Tsias, A., Peter, T., 2000. Water Activity as the Determinant for Homogeneous Ice Nucleation in Aqueous Solutions, pp. 611–614.

Kursinski, E.R., Hajj, G.A., Schofield, J.T., Linfield, R.P., Hardy, K.R., 1997. Observing Earth's atmosphere with radio occultation measurements using the global positioning system. J. Geophys. Res. Atmos. 102, 23429–23465. https://doi.org/10.1029/97jd01569.

Lee, K.O., Dauhut, T., Chaboureau, J.P., Khaykin, S., Krämer, M., Rolf, C., 2019. Convective hydration in the tropical tropopause layer during the StratoClim aircraft campaign: pathway of an observed hydration patch. Atmos. Chem. Phys. 19, 11803–11820. https://doi.org/10.5194/acp-19-11803-2019.

Ma, D., Bian, J., Li, D., Bai, Z., Li, Q., Zhang, J., Wang, H., Zheng, X., Hurst, D.F., Vömel, H., 2022. Mixing characteristics within the tropopause transition layer over the Asian summer monsoon region based on ozone and water vapor sounding data. Atmos. Res. 271 https://doi.org/10.1016/j.atmosres.2022.106093.

Mahnke, C., Weigel, R., Cairo, F., Vernier, J., Afchine, A., Krämer, M., Mitev, V., Matthey, R., Viciani, S., D'Amato, F., Ploeger, F., Deshler, T., Borrmann, S., 2021. The ATAL within the 2017 Asian Monsoon Anticyclone: microphysical aerosol properties derived from aircraft-borne in situ measurements. Atmos. Chem. Phys. Discuss. 21, 15259–15282. https://doi.org/10.5194/acp-2020-1241.

Mehta, S.K., Krishna Murthy, B.V., Narayana Rao, D., Venkat Ratnam, M., Parameswaran, K., Rajeev, K., Suresh Raju, C., Rao, K.G., 2008. Identification of tropical convective tropopause and its association with cold point tropopause. J. Geophys. Res. Atmos. 113, 2–9. https://doi.org/10.1029/2007JD009625.

Nandan, Renju, VenkatRatnam, M., RaviKiran, V., Naik, Dinesh N., 2022. Retrieval of cloud liquid water path using radiosonde measurements: comparison with MODIS and ERA5. J. Atmos. Sol. Terr. Phys. 227 https://doi.org/10.1016/j.jastp.2021.105799.

Narendra Reddy, N., Venkat Ratnam, M., Basha, G., Ravikiran, V., 2018. Cloud vertical structure over a tropical station obtained using long-term high-resolution radiosonde measurements. Atmos. Chem. Phys. 18, 11709–11727. https://doi.org/10.5194/acp-18-11709-2018.

Pan, L.L., Honomichl, S.B., Kinnison, D.E., Abalos, M., Randel, W.J., Bergman, J.W., Bian, J., 2016. Transport of chemical tracers from the boundary layer to stratosphere associated with the dynamics of the asian summer monsoon, 159-14 J. Geophys. Res. 121 (14). https://doi.org/10.1002/2016JD025616, 174.

Pandit, A.K., Gadhavi, H., Ratnam, M.V., Jayaraman, A., Raghunath, K., Rao, S.V.B., 2014. Characteristics of cirrus clouds and tropical tropopause layer: seasonal variation and long-term trends. J. Atmos. Sol. Terr. Phys. 121, 248–256. https://doi.org/10.1016/j.jastp.2014.07.008.

Park, M., Randel, W.J., Emmons, L.K., Bernath, P.F., Walker, K.A., Boone, C.D., 2008. Chemical isolation in the Asian monsoon anticyclone observed in Atmospheric Chemistry Experiment (ACE-FTS) data. Atmos. Chem. Phys. 8, 757–764. https://doi.org/10.5194/acp-8-757-2008.

Park, M., Randel, W.J., Kinnison, D.E., Emmons, L.K., Bernath, P.F., Walker, K.A., Boone, C.D., Livesey, N.J., 2013. Hydrocarbons in the upper troposphere and lower stratosphere observed from ACE-FTS and comparisons with WACCM. J. Geophys. Res. Atmos. 118, 1964. https://doi.org/10.1029/2012JD018327, 1980.

Pruppacher, H.R., Klett, J.D., 1980. Microphysics of clouds and precipitation. Nature 284, 88. https://doi.org/10.1038/284088b0.

Randel, W.J., Wu, F., Forster, P., 2007. The extratropical tropopause inversion layer: global observations with GPS data, and a radiative forcing mechanism. J. Atmos. Sci. 64, 4489–4496. https://doi.org/10.1175/2007JAS2412.1.

Randel, W.J., Park, M., Emmons, L., Kinnison, D., Bernath, P., Walker, K.A., Boone, C., Pumphrey, H., 2010. Asian monsoon transport of pollution to the stratosphere. Science 328 (80), 611–614.

Rao, D.N., Ratnam, M.V., Mehta, S., Nath, D., Basha, S.G., Rao, V.V.M.J., Murthy, B.V.K., Tsuda, T., Nakamura, K., 2009. Val i da tion of the COS MIC Ra dio Occultation Data over Gadanki (13 . 48 ° N , 79 . 2 ° E): a Trop i cal Re gion. Terr. Atmos. Ocean Sci. 20, 59–70. https://doi.org/10.3319/TAO.2008.01.23.01(F3C)1.

Ratnam, M.V., Pravallika, N., Ravindra Babu, S., Basha, G., Pramitha, M., Krishna Murthy, B.V., 2014. Assessment of GPS radiosonde descent data. Atmos. Meas. Tech. 7, 1011–1025. https://doi.org/10.5194/amt-7-1011-2014.

Santee, M.L., Manney, G.L., Livesey, N.J., Schwartz, M.J., Neu, J.L., Read, W.G., 2017. A comprehensive overview of the climatological composition of the Asian summer monsoon anticyclone based on 10 years of Aura Microwave Limb Sounder measurements. J. Geophys. Res. 122, 5491–5514. https://doi.org/10.1002/2016JD026408.

Schoeberl, M.R., Jensen, E.J., Pfister, L., Ueyama, R., Wang, T., Selkirk, H., Avery, M., Thornberry, T., Dessler, A.E., 2019. Water vapor, clouds, and saturation in the tropical tropopause layer. J. Geophys. Res. Atmos. 124, 3984–4003. https://doi.org/10.1029/2018JD029849.

Son, Seok-Woo, Polvani, L.M., 2007. Dynamical formation of an extra-tropical tropopause inversion layer in a relatively simple general circulation model. Geophys. Res. Lett. 34.

Sunilkumar, S.V., Muhsin, M., Emmanuel, M., Ramkumar, G., Rajeev, K., Sijikumar, S., 2016. Balloon-borne cryogenic frost-point hygrometer observations of water vapour in the tropical upper troposphere and lower stratosphere over India: first results. J. Atmos. Sol. Terr. Phys. 140, 86–93. https://doi.org/10.1016/j.jastp.2016.02.014.

Sunilkumar, S.V., Muhsin, M., Venkat Ratnam, M., Parameswaran, K., Krishna Murthy, B. V., Emmanuel, M., 2017. Boundaries of tropical tropopause layer (TTL): a new perspective based on thermal and stability profiles. J. Geophys. Res. 122, 741–754. https://doi.org/10.1002/2016JD025217.

Thomason, L.W., Vernier, J.P., 2013. Improved SAGE II cloud/aerosol categorization and observations of the Asian tropopause aerosol layer: 1989-2005. Atmos. Chem. Phys. 13, 4605–4616. https://doi.org/10.5194/acp-13-4605-2013.

Vernier, J.P., Pommereau, J.P., Garnier, A., Pelon, J., Larsen, N., Nielsen, J., Christensen, T., Cairo, F., Thomason, L.W., Leblanc, T., McDermid, I.S., 2009. Tropical Stratospheric aerosol layer from CALIPSO Lidar observations. J. Geophys. Res. Atmos. 114, 1–12. https://doi.org/10.1029/2009JD011946.

Vernier, J.P., Thomason, L.W., Kar, J., 2011. CALIPSO detection of an Asian tropopause aerosol layer. Geophys. Res. Lett. 38, 1–6. https://doi.org/10.1029/2010GL046614.

Vernier, J.P., Fairlie, T.D., Natarajan, M., Wienhold, F.G., Bian, J., Martinsson, B.G., Crumeyrolle, S., Thomason, L.W., Bedka, K.M., 2015. Increase in upper tropospheric and lower stratospheric aerosol levels and its potential connection with Asian pollution. J. Geophys. Res. 120, 1608–1619. https://doi.org/10.1002/2014JD022372.

Vernier, J.-P., Fairlie, T.D., Deshler, T., Ratnam, M.V., Gadhavi, H., Kumar, S., Natarajan, M., Pandit, A.K., Raj, S.T., Kumar, A.H., Jayaraman, A., Singh, A.K., Rastogi, N., Sinha, P.R., Kumar, S., Tiwari, S., Wegner, T., Baker, N., Vignelles, D., Stenchikov, G., Shevchenko, I., Smith, J., Bedka, K., Kesarkar, A., Singh, V., Bhate, J., Ravikiran, V., Rao, M.D., Ravindrababu, S., Patel, A., Vernier, H., Wienhold, F.G., Liu, H., Knepp, T., Thomason, L., Crawford, J., Ziemba, L., Moore, J., Crumeyrolle, S., Williamson, M., Berthet, G., Jégou, F., Renard, J.B., 2018. BATAL: the balloon measurement campaigns of the asian tropopause aerosol layer. A. Bull. Am. Meteorol. Soc. 99, 955–973. https://doi.org/10.1175/BAMS-D-17-0014.1.

Vogel, B., Günther, G., Müller, R., Grooß, J.U., Riese, M., 2015. Impact of different Asian source regions on the composition of the Asian monsoon anticyclone and of the extratropical lowermost stratosphere. Atmos. Chem. Phys. 15, 13699–13716. https://doi.org/10.5194/acp-15-13699-2015.

Vogel, B., Müller, R., Günther, G., Spang, R., Hanumanthu, S., Li, D., Riese, M., Stiller, G., 2019. Lagrangian simulations of the transport of young air masses to the top of the Asian monsoon anticyclone and into the tropical pipe. Atmos. Chem. Phys. 19, 6007–6034. https://doi.org/10.5194/acp-2018-724.

Vömel, H., David, D.E., Smith, K., 2007. Accuracy of tropospheric and stratospheric water vapor measurements by the cryogenic frost point hygrometer: instrumental details and observations. J. Geophys. Res. Atmos. 112, 1–14. https://doi.org/10.1029/2006JD007224.

Winker, D.M., Vaughan, M.A., Omar, A., Hu, Y., Powell, K.A., Liu, Z., Hunt, W.H., Young, S.A., 2009. Overview of the CALIPSO mission and CALIOP data processing algorithms. J. Atmos. Ocean. Technol. 26, 2310–2323. https://doi.org/10.1175/2009JTECHA1281.1.

World Meteorological Organization, 1957. Definition of the tropopause. World Meteorol. Organ. Bull. 6 (136).

Yu, P., Rosenlof, K.H., Liu, S., Telg, H., Thornberry, T.D., Rollins, A.W., Portmann, R.W., Bai, Z., Ray, E.A., Duan, Y., Pan, L.L., Toon, O.B., Bian, J., Gao, R.S., 2017. Efficient transport of tropospheric aerosol into the stratosphere via the Asian summer monsoon anticyclone. Proc. Natl. Acad. Sci. U.S.A. 114, 6972–6977. https://doi.org/10.1073/pnas.1701170114.

Zhang, Q., Wu, G., Qian, Y., 2002. The bimodality of the 100 hPa South Asia High and its relationship to the climate anomaly over East Asia in summer. J. Meteorol. Soc. Japan 80, 733–744. https://doi.org/10.2151/jmsj.80.733.